PHYSICAL REVIEW C
NUCLEAR PHYSICS

THIRD SERIES, VOLUME 33, NUMBER 4 APRIL 1986

Coupled-channel analysis of nucleon scattering from ^{40}Ca up to 80 MeV

G. M. Honoré, W. Tornow, C. R. Howell, R. S. Pedroni, R. C. Byrd, and R. L. Walter
Department of Physics, Duke University, Durham, North Carolina 27706
and Triangle Universities Nuclear Laboratory, Duke Station, Durham, North Carolina 27706

J. P. Delaroche
Centre d'Etudes de Bruyères-le-Châtel, Serivce de Physique et Techniques Nucléaires, 91680 Bruyères-le-Châtel, France
and Triangle Universities Nuclear Laboratory, Duke Station, Durham, North Carolina 27706
(Received 12 September 1985)

Differential cross sections $\sigma(\theta)$ and analyzing powers $A_y(\theta)$ for neutron scattering to the ground and first 3^- excited state of ^{40}Ca have been measured in the energy range from 11 to 17 MeV. Elastic and inelastic scattering measurements have been obtained for $A_y(\theta)$ at energies of 11.0, 13.9, and 16.9 MeV, the inelastic scattering data representing the first (n,n') measurements of $A_y(\theta)$ for this nucleus. Differential cross sections for (n,n) and (n,n') have been obtained at 13.9 and 16.9 MeV. Both the $\sigma(\theta)$ and $A_y(\theta)$ data at 13.9 MeV have been compared with previous measurements at this energy and the agreement is good, typically within less than 3%. These results have been combined with other $\sigma(\theta)$ and $A_y(\theta)$ data and total cross section σ_T measurements to form a large set of scattering and reaction data for incident energies up to 80 MeV. This data set, along with $\sigma(\theta)$ and $A_y(\theta)$ measurements available for proton scattering in this energy range, has been described in the framework of the coupled-channel formalism. This highly constrained analysis has led to a precise determination of geometries, energy dependencies, and deformation parameters. Further analyses, which dealt with simultaneous couplings to low- and high-energy excited states, have led to improved descriptions of the elastic scattering measurements for $\sigma(\theta)$ and $A_y(\theta)$ at backward angles. These results confirm that real and virtual excitations of giant resonances cannot be ignored in the description of the reaction mechanism. In this context, it has also been found that corrections to the real central potentials, as estimated by Mahaux and Ngô from dispersion relations, help to further improve the fits to elastic scattering observables.

I. INTRODUCTION

One of the issues in nucleon-nucleus scattering studies is the determination of the properties—geometries, energy dependencies, and deformation parameters—of the phenomenological, local, complex optical model potential (OMP). Until recently, the gross properties of the OMP have been deduced mainly from proton scattering measurements performed for a variety of spherical and deformed nuclei up to intermediate energies. Rare are the OMP analyses which have dealt simultaneously with both neutron and proton scattering from a single nucleus and over a broad energy range, partly because of the lack of precise and systematic neutron scattering experiments at incident energies E beyond 30 MeV.

Since ^{40}Ca has been one of the most popular target nuclei used in nucleon scattering studies, many scattering and reaction data are available up to at least 80 MeV. This wealth of data makes ^{40}Ca an attractive candidate for studying the nucleon-nucleus OMP over a wide energy range.

Such an investigation is the main subject of the present work. The OMP analysis concentrates on measurements available at incident energies below 80 MeV. The reason for ignoring the proton scattering measurements available beyond 80 MeV is that the nonrelativistic OMP model that we are using might not be appropriate in the intermediate energy range.[1]

In order to supplement the existing neutron-scattering data base for incident energies between 10 and 20 MeV, an important region for observing the interplay between surface and volume absorption, additional neutron scattering measurements have been performed. Differential cross sections $\sigma(\theta)$ and analyzing powers $A_y(\theta)$ for elastic scattering and inelastic scattering to the first 3^- excited state have been measured at 11.0, 13.9, and 16.9 MeV.

 ©1986 The American Physical Society

The experimental setup as well as data reduction are briefly presented in Sec. II. All the neutron scattering measurements available for $\sigma(\theta)$ and $A_y(\theta)$ at incident energies between 10 and 40 MeV, as well as σ_T measurements reported up to 80 MeV, have been combined in a coupled-channel (CC) analysis. This study, based on the vibrational model, is described in Sec. III A. In Sec. III B, the neutron OMP is converted into a proton OMP. Slight modifications to the OMP parameters are necessary to achieve the best overall representation of both neutron and proton scattering observables. Since ^{40}Ca is a $T=0$ nucleus, symmetry terms do not enter into the model and the neutron and proton OMP well depths differ only by Coulomb correction terms. Accordingly, it is possible to determine whether the magnitude and variation with incident energy of the imaginary Coulomb correction term, as estimated from CC calculations, differs significantly from those derived earlier from spherical optical model (SOM) analyses.[2,3] Another outcome of the present work is that one can compare directly the vibrational amplitudes determined from the (n,n′) and (p,p′) scattering analyses.

Although the overall description of the scattering observables is reasonably good, systematic deviations between the CC predictions and elastic scattering measurements for $\sigma(\theta)$ and $A_y(\theta)$ exist at backward angles. In order to improve the description of the elastic scattering pattern in this region, CC calculations including couplings to identified $E2$ and $E3$, $T=0$ giant resonances have been performed. These calculations require that the potentials in the incoming and outgoing channels be properly evaluated, especially in the energy range where dispersion relation corrections to the real part of the optical potential are significant.[4] This study is presented in Sec. III C.

II. EXPERIMENT

A. Analyzing power measurements

The neutron analyzing power measurements $A_y(\theta)$ reported in this work at 10.96, 13.90, and 16.92 MeV were made at Triangle Universities Nuclear Laboratory (TUNL) using pulsed-beam neutron time-of-flight (TOF) techniques. Analyzing powers for elastic scattering have been measured to within absolute uncertainties of between 0.02 and 0.05, and the inelastic scattering measurements have typical uncertainties of between 0.04 and 0.07. The arrangement of gas target, scatterer, and detectors was similar to that described in Ref. 3. A deuteron beam from the Lamb shift polarized ion source was pulsed and then injected into the FN tandem Van de Graaff accelerator. Beam polarization, as measured by the quench-ratio method, was typically $p_z=0.7$. After acceleration, the beam was directed through a 6.35 μm Havar foil into a deuterium-filled gas cell 3.16 cm long. Deuterium gas pressure was typically maintained at 7.7 bar during these measurements. Polarized neutrons were produced via the polarization-transfer reaction ^{2}H($\vec{d}$, $\vec{n}$)^{3}He at $\theta=0°$.

The calcium scattering sample was a right circular cylinder, 2.5 cm in height and 2.5 cm in diameter. This sample was suspended upon a thin wire with its axis of symmetry perpendicular to the scattering plane. The scatterer was composed of elemental calcium, which is 96.9% ^{40}Ca.

Neutrons scattered by the sample were detected with two heavily-shielded NE-218 liquid scintillators located in the horizontal reaction plane. The center-to-center distances from the sample to the left and right detectors were, respectively, 5.7 m and 3.7 m at all energies. Time-averaged beam currents, as measured at the deuterium gas cell, were between 100 and 140 nA. Thresholds were set electronically in each detector so that pulses with amplitudes smaller than those associated with γ rays from the Compton edge of ^{137}Cs were rejected. In addition to each detector's intrinsic shielding of paraffin and lithium carbonate, tapered shadow bars of both copper and tungsten were used to occlude the view of the direct neutron source.

Measurements were made with left and right detectors set at equal reaction angles, using the "two-detector, spin-flip" method. Scattered neutrons were identified via fast timing signals from the detectors and the capacitive pickoff for the pulsed deuteron beam. Standard TOF electronics were employed, and γ-ray events were excluded from the TOF spectra by pulse-shape discrimination methods. Figure 1(a) shows typical spectra for the right detector at our highest incident energy, $E_n=16.9$ MeV, at laboratory angles of $\theta=45°$ and 150°. The spectra shown are the calculated differences between measurements made with the sample in place and corresponding spectra obtained with the sample replaced by a bare sample hanger, i.e., a sample-out configuration. Neutron TOF increases from right to left. The peak seen at far right is due to elastic scattering. Inelastic scattering to the low-lying 3^- ($E_x=3.74$ MeV), 2^+ ($E_x=3.90$ MeV), and 5^- ($E_x=4.49$ MeV) levels in ^{40}Ca are seen as a broad peak around channel 350 in the 150° spectrum. The choice of windows is indicated in the figure. Events that correspond to inelastic scattering to a particular excited state are not completely resolved at any angle. The method of extraction of $A_y(\theta)$ data was dictated in large part by this fact, and is explained in Sec. II C below.

B. Differential cross section measurements

The measurements of neutron differential cross sections $\sigma(\theta)$ reported here at 13.90 and 16.92 MeV were performed with an experimental arrangement identical to that described above for $A_y(\theta)$, except that unpolarized incident deuterons were used to produce unpolarized neutrons at $\theta=0°$. The relative uncertainties in the elastic scattering cross sections are typically between 2% and 3%, and less than 5% in the inelastic scattering case. A third liquid scintillator, suspended above the deuterium gas cell, was used to monitor the primary neutron source for normalization purposes. The yields were further normalized to obtain absolute differential cross sections using periodic measurements for n-p scattering from hydrogen in a well-characterized polyethylene sample and published n-p scattering cross sections.

Figure 1(b) shows typical time-of-flight spectra for the 3.7 m detector at $E_n=16.9$ MeV for angles $\theta=55°$ and

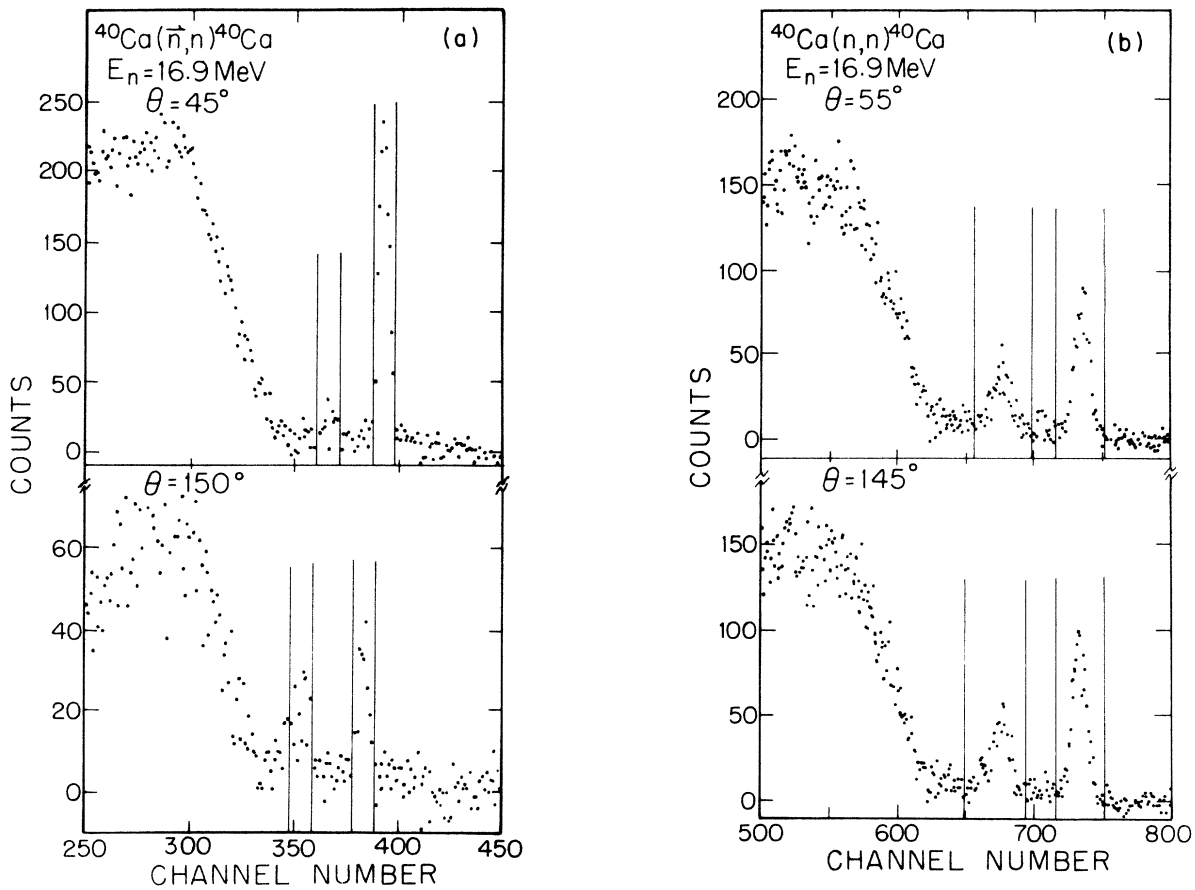

FIG. 1. (a) Time-of-flight spectra for 16.9 MeV polarized neutrons scattered from calcium through laboratory angles of $\theta=45°$ and $\theta=150°$. Time increases from right to left. The figure indicates the windows used for extracting elastic and inelastic scattering cross sections (see Sec. II C). (b) Time-of-flight spectra for 16.9 MeV unpolarized neutrons scattered from calcium through laboratory angles of $\theta=55°$ and $\theta=145°$. Time increases from right to left. The figure indicates the windows used to extract analyzing powers for elastic and inelastic scattering (see Sec. II C).

$\theta=145°$. The description is similar to that of Fig. 1(a) in Sec. II A above. The method of data extraction is described below.

C. Data reduction and corrections

It can be seen in Figs. 1(a) and (b) that the resolution of the TOF spectrometer was not sufficient to resolve the group of excited states 3^-, 2^+, and 5^- in the TOF spectra. We chose to extract information about these states in the following manner: In the case of cross sections, windows were set to include neutrons scattered to all three states, giving a yield that was then converted to a combined (3^-, 2^+, 5^-) cross section. No evidence of excitation of the low-lying 0^+ state was seen. In order to obtain more detailed information from the polarization measurements, we took advantage of the fact that $A_y(\theta)$ is a ratio, and we were therefore not constrained to include all events from any particular reaction, as long as we consistently used the same window for the spin-up as for the spin-down configuration. This allowed us to set windows that excluded most events due to scattering to the 5^- state. Due to the large uncertainties, analyzing power data for this state could not be used in the analysis. The overlap of peaks from the 2^+ and 3^- excited states is so complete that an analyzing power was calculated only for the sum of these peaks.

No attempt was made to further reduce either the cross sections or analyzing powers extracted by this method to their individual constituents. However, in the coupled-channel analysis, calculations of the observables were made for the individual states and a weighted sum was compared to the data. In the case of the $\sigma(\theta)$ data from Ref. 5 at 11.0 and 20.0 MeV, cross sections for the resolved 3^- state (as well as 2^+ and 5^- at 11.0 MeV) were available. We compared our CC calculations at these energies and found the agreement to be good, giving increased confidence in the systematics of our summed calculations.

The observables $\sigma(\theta)$ and $A_y(\theta)$ are defined in theory for scattering from a point sample into a point detector. Corrections for the finite geometry of the sample and apparatus, as well as for multiple scattering were made to both sets of data. The differential cross sections were corrected using the Monte Carlo code EFFIGY15, developed at TUNL, which corrects for relative detector efficiency and attenuation in the sample as well. The corrections to $A_y(\theta)$ are considerably more involved. The

Monte Carlo code JANE, which was written in part by one of the authors (W.T.) at the Universität Tübingen, was used for this task.

III. COUPLED-CHANNEL ANALYSIS

A. Neutron + ^{40}Ca potential

Since the first 3^- ($E_x = 3.74$ MeV) excited state has not been resolved from the neighboring 2^+ ($E_x = 3.90$ MeV) and 5^- ($E_x = 4.49$ MeV) levels in the measurements performed in our laboratory at 11.0, 13.9, and 16.9 MeV, the coupling scheme (0^+, 3^-, 2^+, 5^-) has been assumed in the CC calculations. All calculations were conducted using the computer code ECIS79, written by Raynal.[6] The excited 0^+ ($E_x = 3.35$ MeV) level was not considered since it is not actually a collective state.[7] The other states treated explicitly in the calculations are assumed to be surface vibrations and are represented as such in a first-order vibrational model.[8] The central and noncentral transition potentials are assumed to be complex, and relativistic kinematics are used in the calculations for $E > 30$ MeV. The net effect of relativistic compared to nonrelativistic kinematics is to increase the CC predictions for σ_T by a few percent, and to slightly alter the shape and phase of the predicted angular distributions. Finally, the CC calculations are conducted in such a way that the deformation lengths δ_λ ($\delta_\lambda = \beta_\lambda R$, where $\lambda = 2$, 3, and 5) have identical values for all λ-transition terms in the OMP. The deformed optical potential U, using standard notation,[9,10] is written as follows:

$$U = -Vf(r,R_v,a_v) - iW_v f(r,R_d,a_d) + i4a_d W_d \frac{df}{dr}(r,R_d,a_d) - 2i\lambda_\pi^2 (V_{so} + iW_{so}) \nabla f(r,R_{so},a_{so}) \times \nabla \cdot s \ ,$$

where the form factors are of the Woods-Saxon—type

$$f(r,R_i,a_i) = \{1 + \exp[(r - R_i)/a_i]\}^{-1} \ ,$$

with

$$R_i = r_i A^{1/3} \left[1 + \sum_{\lambda\mu} \alpha_{\lambda\mu} Y_{\lambda\mu} \right], \quad \lambda = 2,3,5 \ ,$$

and the vibration amplitudes β_λ are related to the phonon operators $\alpha_{\lambda\mu}$ as defined in Ref. 8.

The data base consisted of measurements performed in several laboratories. The σ_T data were taken from Refs. 11 and 12, and the published $A_y(\theta)$ and $\sigma(\theta)$ measurements were obtained from Refs. 3, 5, and 13. The new TUNL $\sigma(\theta)$ and $A_y(\theta)$ measurements were important for determining the features of the spin-orbit potential and for providing more guidance in mapping the interplay between surface (W_d) and volume (W_v) absorption. The σ_T measurements[12] at incident energies between 70 and 80 MeV were very useful in establishing the proper balance between W_d and W_v, so that the volume integral of surface plus volume absorption does not display any pathological behavior as E increases up to 80 MeV.

We have assumed simple functional forms to represent the variation with energy of the potential depths (see Table I). A linear variation with energy seems to be a reasonable assumption for the real central potential V. We have identified the need of a non-negligible strength for the volume absorption potential above a critical incident energy. This critical energy is not well defined in cases where the $\sigma(\theta)$ data are scarce in the 10—30 MeV energy range. Some data in this region are indeed available for ^{40}Ca. For this nucleus, the optimum value attributed to the critical energy is 20 MeV, and we estimated the uncertainty in this figure to be ± 2 MeV. The reason for attributing this relatively large uncertainty is the inherent ambiguity in the interplay between surface and volume absorption at these energies. This ambiguity could perhaps be resolved if more $\sigma(\theta)$ measurements were available between 17 and 26 MeV. It is also related to our oversimplified representation of the reaction mechanism (see Sec. III C), which restricted us from fully exploiting the sensitivity of the backward angle region of $\sigma(\theta)$ for elastic scattering to W_d and W_v. According to our parametrization, the surface absorption vanishes at an incident energy of 66 MeV, but clearly this figure is not well defined. Additional differential measurements will be needed above 40 MeV to trace more precisely the interplay between W_d and W_v above 20 MeV (see Sec. III B).

On the other hand, we found that the real part V_{so} of the spin-orbit interaction is nearly E independent (see

TABLE I. Neutron + ^{40}Ca optical potential parameters. Potential depths are in MeV; geometrical parameters in fm. Relativistic kinematics are used above 30 MeV.

$V = 50.1 - 0.254E$	$(0 \le E \le 80)$
$W_v = 0.0$	$(0 \le E \le 20)$
$W_v = 0.16(E - 20)$	$(20 \le E \le 80)$
$W_d = 3.72 + 0.18E$	$(0 \le E \le 20)$
$W_d = 7.32 - 0.16(E - 20)$	$(20 \le E \le 80)$
$V_{so} = 5.42 - 0.024E$	$(0 \le E \le 80)$
$W_{so} = 0.600$	$(0 \le E \le 80)$
$r_v = 1.25 \quad r_d = 1.25 \quad r_{so} = 1.02$	
$a_v = 0.65 \quad a_d = 0.58 \quad a_{so} = 0.50$	
$\beta_v(3^-) = 0.329 \quad \beta_v(2^+) = 0.088 \quad \beta_v(5^-) = 0.243$	

Table I), as predicted by nuclear matter calculations.[14] When comparing the geometries of the real spin-orbit potential as deduced from the present analysis to those from an earlier SOM analysis[3] of ^{40}Ca in a restricted energy range, in which $a_{so}=0.27$ fm, one notices that this diffuseness takes on a quite different value from that obtained in the SOM work. The enlarged energy range in conjunction with the CC description helps to restore a more physical value for a_{so}, that is close to values found empirically when parametrizing charge distributions.[15] We checked that our representation of the spin-orbit potential makes sense by performing CC calculations in which we used a semimicroscopic spin-orbit potential, derived[16] from Hartree-Fock point proton and neutron densities,[17] and found that the $A_y(\theta)$ predictions barely deviate from the above results.[18]

We found that the full spin-orbit potential needs to be complex at incident energies between 10 and 17 MeV, but found no clear evidence that it should be deformed. In this energy range the imaginary part of the so potential has a depth W_{so} estimated to be between $+1.0$ and $+0.5$ MeV. As there are no $A_y(\theta)$ data available for neutrons at higher energies, an accurate determination of the energy dependence of W_{so} was not possible; therefore

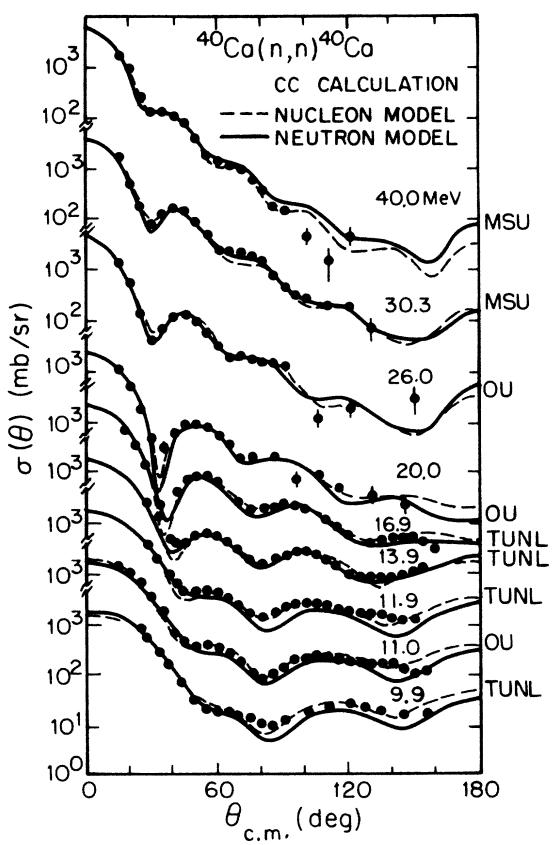

FIG. 2. Neutron elastic scattering from ^{40}Ca. The laboratories of origin are indicated at right. Comparison of the elastic scattering measurements for $\sigma(\theta)$ (dots) and CC calculations (solid and dashed curves) described in Sec. III. The measurements are from the present work at 13.9 and 16.9 MeV, and from Refs. 3, 5, and 13.

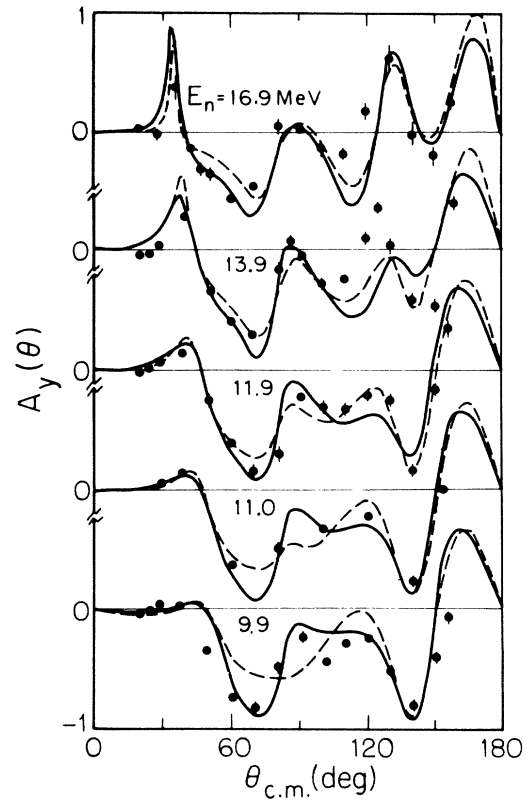

FIG. 3. Neutron elastic scattering from ^{40}Ca for $A_y(\theta)$. For other comments, see the caption of Fig. 2. The data are from the present work at 11.0, 13.9, and 16.9 MeV, and from Ref. 3.

W_{so} was taken to be energy independent for the model in this section. The optimum value for W_{so} (see Table I) is positive, a result at variance with model predictions[1,14] and experimental evidence for proton scattering at higher incident energies,[19] but in keeping with other TUNL results for spherical nuclei.[20] This energy dependence is reexamined in Sec. III B.

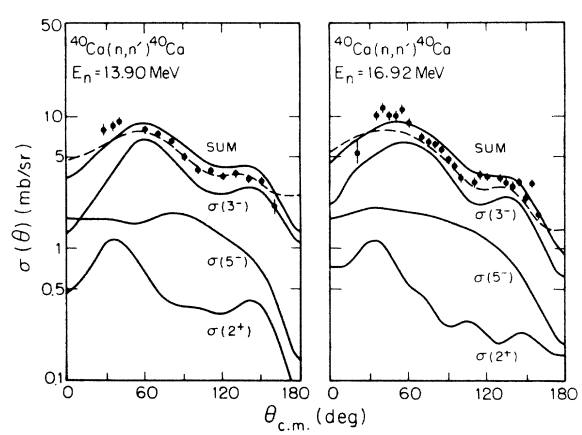

FIG. 4. Neutron inelastic scattering to the first 3^- state of ^{40}Ca. The $\sigma(\theta)$ data are from the present work. The figure shows how the CC calculations of Sec. III A (solid curves) for $\sigma(3^-)$, $\sigma(5^-)$, and $\sigma(2^+)$ add up to represent the unresolved $\sigma(3^-)$ measurements. The dashed curves represent the CC prediction from Sec. III B of the combined contributions.

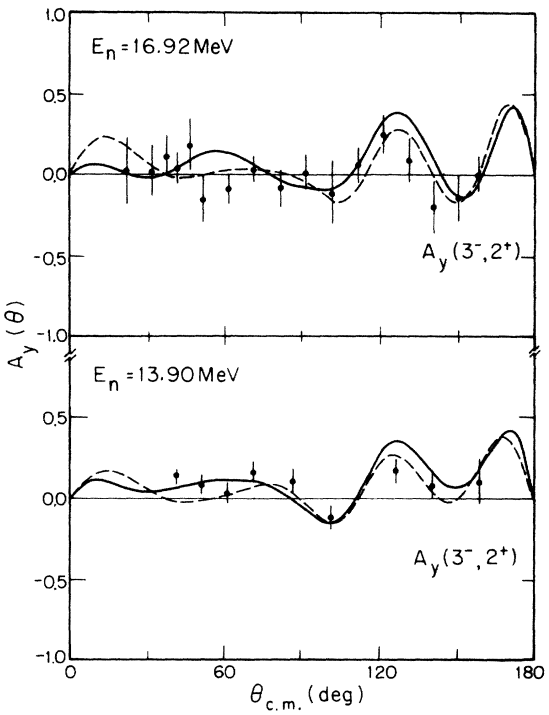

FIG. 5. Neutron inelastic scattering to the first 3^- state of ^{40}Ca. The $A_y(\theta)$ data are from the present work. The contributions from $A_y(2^+)$ and $A_y(3^-)$, as predicted in our modeling, are summed according to the cross section weights in order to compare to the unresolved measurements. The solid and dashed curves are CC calculations described in Secs. III A and III B, respectively.

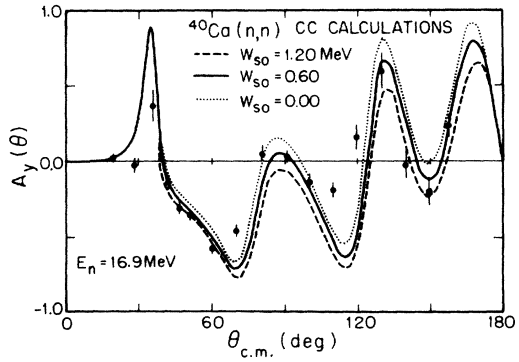

FIG. 6. Sensitivity of $A_y(\theta)$ to the imaginary spin-orbit potential W_{so} for neutron elastic scattering from ^{40}Ca at $E_n = 16.9$ MeV. Calculations are shown with W_{so} equal to the optimum value (solid curve), twice the optimum value (dashed curve), and zero (dotted curve). The OMP parameters are from Table I.

A comparison between the present predictions and σ_T data[12] between 500 keV and 80 MeV has been reported earlier.[21] There is a good overall agreement, to within 3% between the calculations and these measurements, as well as with the energy-averaged representation of the σ_T data[11] down to 500 keV.

The calculations for the observables $\sigma(\theta)$ and $A_y(\theta)$ are shown as solid curves in Figs. 2–5. The overall agreement between the measurements and the curves is reasonably good. In particular, the agreement achieved in the present work at 11 and 20 MeV for the 3^- $\sigma(\theta)$ data as well as for the 5^- $\sigma(\theta)$ data at 11 MeV is as good as that of the DWBA analysis in Ref. 5. Without compromising the agreement at 11 and 20 MeV, the model description of $\sigma(\theta)$ for the unresolved 3^- state, as measured at 13.9 and 16.9 MeV, can be improved[18] for $\theta > 60°$ by inserting an $E2$ transition[22] from the 3^- and 5^- states in the coupling scheme. However, this effectively changes the collective picture from a linear to an anharmonic vibrational model.

In viewing Figs. 2 and 3, one notices some weakness in our CC calculations. In particular, it can be seen that our predictions for elastic scattering get relatively worse as E decreases from 17 to 10 MeV. The results of Hauser-Feshbach calculations showed that this behavior is not due to compound-elastic effects. It was frustrating to discover that no significant improvement in the description of the 9.9 MeV $\sigma(\theta)$ and $A_y(\theta)$ elastic scattering data is achieved when shifting from a SOM analysis[3] to a CC analysis. Some plausible explanations for the partial failure of our CC predictions are discussed in Sec. III C.

The sensitivity of the analyzing power calculations to the presence of the imaginary so term W_{so} is demonstrated in Fig. 6. This figure compares the 16.9 MeV analyzing power data for neutron elastic scattering to CC calculations made with the optimum value $W_{so} = 0.6$ MeV, and with $W_{so} = 1.2$ MeV, and $W_{so} = 0$. This figure clearly demonstrates the need for the inclusion of this term, as well as the general sensitivity of the data to the presence of W_{so}.

B. Nucleon + ^{40}Ca potential

The existing $\sigma(\theta)$ and $A_y(\theta)$ measurements for p + ^{40}Ca were combined with the neutron data set analyzed in Sec. III A to define a single OMP, valid for both neutrons and protons. The set of proton scattering measurements is specified in Table II. The available measurements[40] for the reaction cross section σ_R have also been used as additional constraints.

It is relatively easy to convert the neutron OMP into a proton OMP for ^{40}Ca, since this is a $T=0$ nucleus; the OMP well depths for neutrons and protons differ only by the complex Coulomb correction term[2,41] ΔU_C ($\Delta U_C = \Delta V_C + i\Delta W_C$) if the geometries are identical for neutron and proton scattering and independent of incident energy.

The OMP parameters determined in Sec. III A do not reproduce the proton data if ΔV_C is set equal to the usual value[2,41] of $0.46Z/A^{1/3}$ (MeV) and ΔW_C is set[2,3] to $\Delta W_C \neq 0$ at incident energies below 45 MeV. In order to describe both sets of data, the geometries had to be modified and the energy dependencies of the potential depths needed to be reoptimized by replacing the functional forms so far assumed for $W_d(E)$ and $W_v(E)$ with more appropriate ones. These functions are shown in Table III. These forms are still somewhat arbitrary but fulfill the requirement that the absorptive potential should not increase without bound with increasing incident energy. They also incorporate the information that the absorptive

TABLE II. Reference list for the p + ^{40}Ca scattering measurements considered in the CC analysis. The symbol x attached to either $\sigma(\theta)$ or $A_y(\theta)$ means that data exist for the observable at a specific incident energy.

E (MeV)	$\sigma(\theta)$	$A_y(\theta)$	Reference
17.5		x	23
18.2		x	24
19.6	x		24
21.0	x	x	24,25
23.5	x		25
24.9[a]	x		26
26.3	x	x	25,27
28.5		x	28
30.0[a]	x		26
30.3	x	x	29,30
34.8[a]	x		26
35.8	x	x	31
39.8[a]	x		26
40.0	x	x	32
45.5	x	x	31
48.0	x		25
49.0		x	33
61.4	x		34
65.0[b]	x	x	35,36
75.0[c]	x	x	37
80.2	x	x	19,39

[a]Measured $\sigma(\theta)$ for inelastic scattering to the 3^- and 5^- low-lying states also exist (Ref. 26).
[b]Data below 90° are from Ref. 35; data above 90° are from Ref. 36.
[c]Data renormalized as suggested by van Oers (Ref. 38).

potential behaves like $(E-\epsilon_F)^2$ near the Fermi energy ϵ_F, as predicted by the Fermi gas model.[4] For the sake of simplicity, the mean value $\bar{\epsilon}_F=\frac{1}{2}[\epsilon_F(\mathrm{n})+\epsilon_F(\mathrm{p})]$ has been assumed throughout ($\bar{\epsilon}_F=-8.5$ MeV).

Comparing the geometries shown in Tables I and III, one sees that they are different. The proton data carried considerably more weight than the neutron data in the combined analysis, due to the greater number of available proton scattering measurements. Since most of the proton scattering data were for energies between 20 and 80 MeV, whereas the neutron scattering data were mainly for energies below 20 MeV, these differences may indicate that assuming E-independent geometries in the whole energy range is not appropriate. For instance, the radius r_v of the real central potential changes from $r_v=1.25$ fm (see Table I) to $r_v=1.23$ fm (see Table III). By looking at the global (p,p) scattering analysis performed by Nadasen *et al.*[39] in the energy range from 80 to 180 MeV, it appears that r_v prefers an even lower value ($r_v\simeq1.21$ fm). Therefore, there is some evidence from our work and that of Ref. 39 that one cannot assume fixed geometries in OMP analysis conducted over a very broad energy range.

Due to the lack of higher-energy neutron data, it is not clear whether an energy dependence of the geometrical parameters would be different for proton and neutron scattering. The somewhat different energy dependencies found for the real and the imaginary central potentials in the neutron + ^{40}Ca and the nucleon + ^{40}Ca analyses might also be caused by the fact that the n + ^{40}Ca analysis relies heavily on data in a very restricted energy range. Although our n + ^{40}Ca analysis was done before the refined nucleon + ^{40}Ca analysis, a satisfactory neutron solution—not optimal from the point of view of chi-squared, however—can be obtained using the same functional forms as in the combined potential. In most cases, the regions of chi-squared minima are quite flat. More accurate neutron data will be required to better determine the parameter values of the n + ^{40}Ca analysis.

Other important results of our combined (n,n) and (p,p) scattering analysis is that the spin-orbit potential must be complex, and β_{so} should be set to zero. Assuming $\beta_{so}\neq0$ produces significant changes in the predictions for $\sigma(\theta)$ and $A_y(\theta)$ and the chi-squared values increase systematically, very often by more than 50%. The potential depth V_{so} is nearly energy independent, as found in Sec. III A. In contrast, W_{so} varies with incident energy as illustrated in Fig. 7. Although the estimated uncertainties attached to the W_{so} values are large, there is a definite tendency for W_{so} to be positive at lower energies and negative at

TABLE III. Nucleon + ^{40}Ca optical potential parameters. Potential depths are in MeV; geometrical parameters in fm. The subscript n indicates that the potential is given as it is defined for neutrons. Potentials without subscript prefixes are common to both neutrons and protons. Relativistic kinematics are used above 30 MeV.

${}_{\mathrm{n}}V=50.66-0.33E$	$(0\le E\le80)$
$\Delta V_C=2.84$ MeV	$(0\le E\le80)$
$W_v=0.0012(E-\bar{\epsilon}_F)^2\exp\{-[0.004(E-\bar{\epsilon}_F)]\}$	$(0\le E\le80)$
${}_{\mathrm{n}}W_d=0.0341(E-\bar{\epsilon}_F)^2\exp\{-[0.0509(E-\bar{\epsilon}_F)]\}$	$(0\le E\le20)$
${}_{\mathrm{n}}W_d=6.50-0.045(E-20)$	$(20\le E\le80)$
$\Delta W_C\neq0.0$ MeV[a]	$(0\le E\le45)$
$V_{so}=5.6-0.008E$	$(0\le E\le80)$
$W_{so}=1.17-0.024E$	$(0\le E\le80)$
$r_v=1.23$ $r_d=1.23$ $r_{so}=1.05$	
$a_v=0.68$ $a_d=0.58$ $a_{so}=0.60$	
$\beta_v(3^-)=0.320$ $\beta_v(2^+)=0.088$ $\beta_v(5^-)=0.210$	

[a]See the text; $0<\Delta W_C<1.6$ MeV.

higher energies, crossing zero around 50 MeV. There exists no nuclear structure model to describe this pattern. On the other hand, the feature that W_{so} is negative at higher incident energies is in agreement with recent (p,p) analyses[19,39] (illustrated as a dashed curve and the symbol $\times$ in Fig. 7) and with the Dirac phenomenology.[1] At lower energies, the W_{so} values deduced from the neutron scattering analysis and the nucleon scattering analysis have comparable magnitudes. This agreement is consistent with the picture that, except for the usual Coulomb correction terms, the n + ^{40}Ca and p + ^{40}Ca optical potentials are identical.

Another finding is that ΔW_C is a surface term. Its depth decreases from 1.6 MeV to zero as E increases from 17 to 45 MeV. These findings are in good agreement with earlier results[2,3] based on SOM analyses, showing that the CC analysis neither removes nor alters the basic behavior of ΔW_C. The energy dependence of ΔW_C, although not complicated, has not been well represented by any obvious analytic function. It has been tabulated but has not been parametrized as yet.

The description of $\sigma(\theta)$ from the OMP parameters of Table III (shown as dashed curves in Figs. 2 and 3) is of comparable quality to that obtained with the parameters of Table I. On the other hand, the new elastic scattering predictions for $A_y(\theta)$ get worse. The results obtained for proton elastic scattering with the OMP parameters of Table III are shown as solid curves in Figs. 8 and 9. The elastic scattering measurements for $\sigma(\theta)$ are well described except at backward angles. Likewise, the predictions for $A_y(\theta)$ (see Fig. 9) are also poor at backward angles, and become even worse at 65 MeV for $\theta > 90°$. Our CC analyses do not help to remove the backward angle anomaly mentioned earlier[42] for a variety of nuclei with mass $A < 70$. In the next section we illustrate how to explain part of this anomaly in the elastic channel.

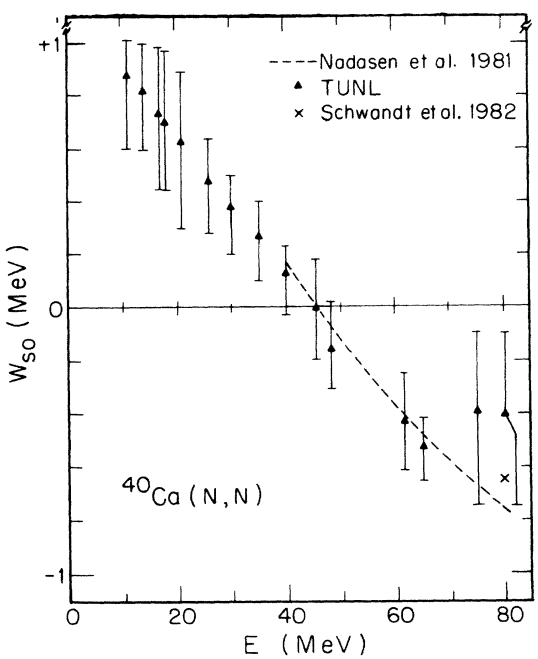

FIG. 7. Variation with incident energy of the imaginary spin-orbit potential depth. The W_{so} values shown above 17 MeV are derived from $A_y(\theta)$ data (Refs. 23–39) for proton scattering. The other W_{so} values are derived from $A_y(\theta)$ data measured at TUNL (present work and Ref. 3) for neutron scattering. The dashed curve is an extrapolation from Ref. 40 and the cross is from Ref. 19.

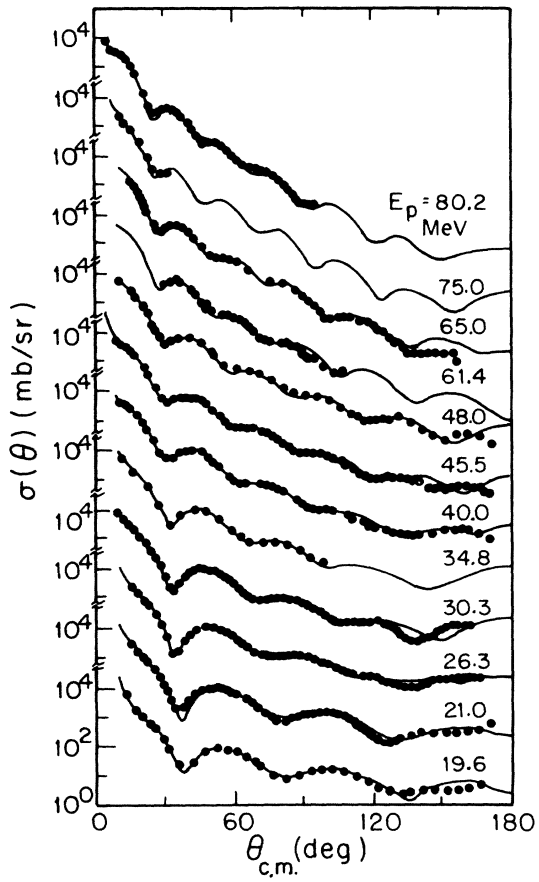

FIG. 8. The (p,p) scattering cross sections for ^{40}Ca. The measurements are from Refs. 23–39. The solid curves represent CC calculations based on the OMP parameters listed in Table III.

The predictions for inelastic scattering observables are reasonably good for both neutrons and protons. These are shown as dashed curves for (n,n′) scattering in Figs. 4 and 5, and as solid curves for (p,p′) scattering to the 3^- and 5^- excited states in Fig. 10. The description (not shown) of the $\sigma(\theta)$ measurements[5] at 11 and 20 MeV for (n,n′) scattering is as good as it is with the parameters of Sec. III A. A comparison between the values of β_3 and β_5 found from (n,n′) and those from (p,p′) scattering analyses shows that within uncertainties of about 5%, $\beta_\lambda(\text{n,n}') = \beta_\lambda(\text{p,p}')$ for $\lambda = 3$ and 5. This result indicates that core-polarization effects are much less important for double-closed-shell nuclei than they are for single-closed-shell nuclei.[43]

C. Coupling to giant resonances and dispersion relation effects

There have been several attempts to improve the description of the nondiffractionlike pattern of the proton

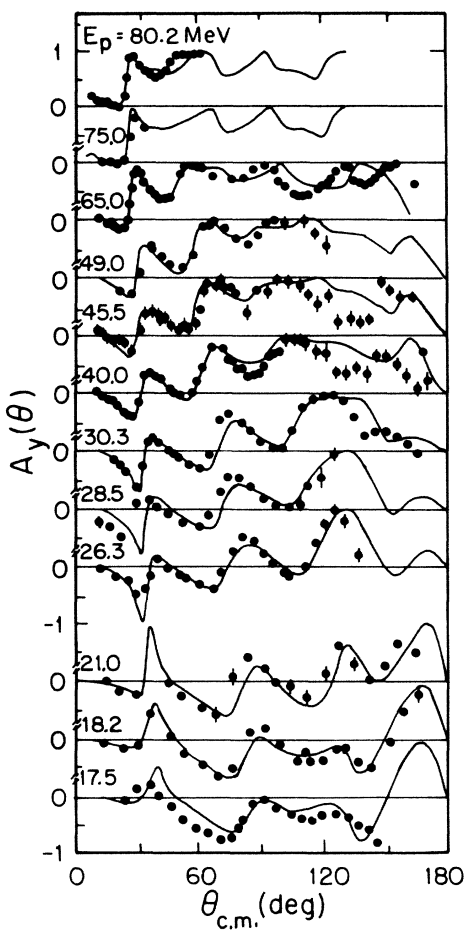

FIG. 9. The (p,p) analyzing powers for ^{40}Ca. See caption of Fig. 8.

elastic scattering cross sections at backward angles for light and medium mass nuclei ($A<70$), including ^{40}Ca. Improved descriptions of $\sigma(\theta)$ have been achieved by considering nonstandard radial form factors,[44] l-dependent potentials,[45] (p,d,p) intermediate processes,[46] model-independent analyses,[47] and coupling to giant resonances.[48] This last work deals with isoscalar giant resonances (IGR's) treated in CC calculations as surface modes of excitation.

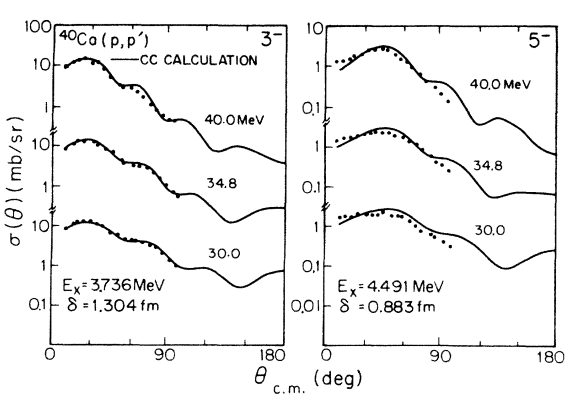

FIG. 10. The (p,p′) scattering cross sections for the 3^- and 5^- excited states. The measurements are from Ref. 26. See the caption of Fig. 8.

In the present analysis, the method outlined in Ref. 48 has been adopted. The sensitivity calculations to be shown below deal with coupling to the $L=2$ ($E_x=17.8\pm0.3$ MeV) and $L=3$ ($E_x=31\pm2$ MeV) IGR states as identified in Refs. 49 and 50. These excited states exhaust 40% and 20% of the energy-weighted sum rules, respectively. Therefore, we have adopted the values β_2 (IGR)$=0.164$ and β_3 (IGR)$=0.138$ and used the coupling scheme (0^+, 3_1^-, 2^+, 3_2^-). Here, the 2^+ and 3_2^- levels are the giant resonances, and 3_1^- is the low-lying ($E_x=3.74$ MeV) octupole state.

Since the local OMP is energy dependent, the real and imaginary potentials in the incoming and outgoing channels have to be properly evaluated at negative as well as positive energies, and, in particular, in the vicinity of the Fermi energy, a region which has been studied at length by Mahaux and Ngô via dispersion relations.[4] At incident energies such that $|E-\bar{\epsilon}_F|<10$ MeV, the corrections to the real central part of the OMP as predicted in Ref. 4 are dominated by surface terms. When E departs from this energy window, the corrections to the real potential change from a surface-dominated to a volume-dominated radial shape. At sufficiently high (positive or negative) energies, these volume correction terms can be absorbed into, and act as renormalization terms for the real part of the semimicroscopic optical potential (the Hartree-Fock term) defined in Ref. 4. In phenomenological OMP analyses, these volume correction terms are implicitly incorporated in the depth of the (Woods-Saxon) real central potential. If the dispersion relation corrections are treated explicitly in the phenomenological OMP analyses, just the surface components of the corrections have to be considered.

We are aware of the existence of few other studies in which dispersion relations have been used in analyses of nucleon-scattering data. A recent attempt to describe nucleon elastic and inelastic scattering from ^{16}O in this manner has been made at Ohio University. The result obtained is a significant improvement in the phasing of the predictions for $\sigma(\theta)$ at backward angles.[51] Smith *et al.* have also explored dispersion-relation corrections to the real potential in their recent (n,n) scattering analysis[52] of ^{93}Nb, by allowing a modification to the function energy dependence of the volume integral of this potential in the Fermi energy region. It is worth noting, however, that these analyses take into account only the effects due to dispersion-relation modifications to the volume integral of the real potential, and ignore effects that are related to the shape of the potential itself.[53]

For ^{40}Ca, we took advantage of the information contained in Ref. 4 on the radial shapes of the corrections to the real part of the neutron OMP. The surface components of the correction terms have been modeled as derivatives of Woods-Saxon shapes and inserted directly into the CC calculations based on the parameters of Table III. The imaginary potentials have been assumed to be symmetric[4] with respect to $\bar{\epsilon}_F$. An illustration is given in Fig. 11 for the incident neutron energy $E_n=16.9$ MeV. There is a definite and significant improvement in the $\sigma(\theta)$ and $A_y(\theta)$ predictions (dashed curves) compared to

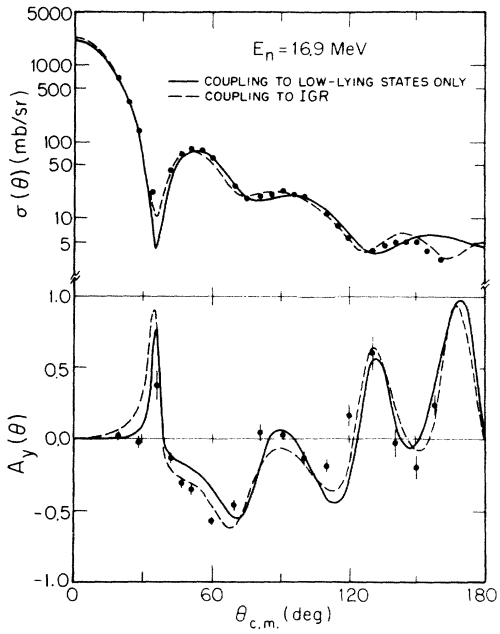

FIG. 11. Comparison of ^{40}Ca(n,n)^{40}Ca data to CC calculations at $E_n = 16.9$ MeV. The solid curve is from the parameters of Table III and includes coupling to low-lying states only (see the text); the dashed curve includes dispersion-relation corrections and coupling to giant resonances.

the CC calculation of Sec. III B (solid curves) in the whole angular range. Still better agreement with the data could be achieved by reoptimizing the potential parameters, for instance, by increasing W_d by about 0.3 MeV. Another example is given for (p,p) scattering at 30.3 MeV in Fig. 12. Here, too, the predictions (dashed curves) are better: comparing the two calculations, the chi-squared drops by

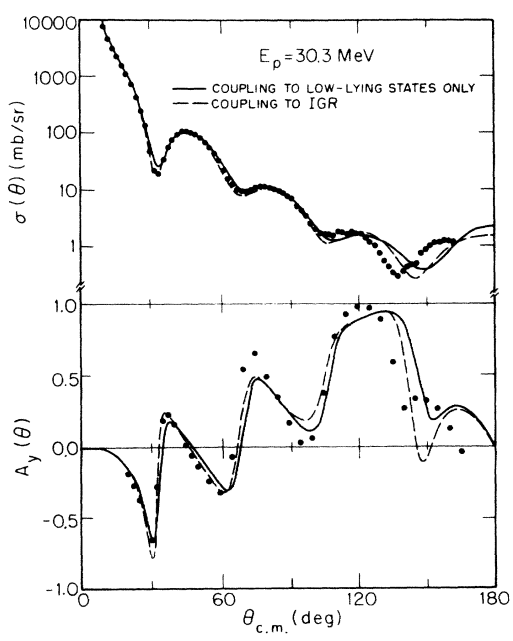

FIG. 12. Comparison of ^{40}Ca(p,p)^{40}Ca data to CC calculations at $E_p = 30.3$ MeV. See the caption of Fig. 11.

60% and 100% for $\sigma(\theta)$ and $A_y(\theta)$, respectively.

More guidance form the OMP theory is required to extend these CC analyses to the whole body of existing scattering measurements. Our preliminary efforts to reanalyze the $\sigma(\theta)$ and $A_y(\theta)$ data in the context of coupling to IGR's systematically indicate that improved fits could be obtained at incident energies up to 50 MeV. Our study indicates that the effect of coupling to giant resonances predominates over dispersion-relation effects at energies below 40–50 MeV. Beyond these energies, coupling to the 2^+ ($E_x = 17.8$ MeV) and 3^- ($E_x = 31$ MeV) giant resonances has minimal effects on the OMP predictions. Obviously, the reason is that we are too far in energy from these resonances. Improving the fits to $\sigma(\theta)$ and $A_y(\theta)$ for (p,p) scattering at 65 MeV, for instance, requires additional information on the existence, location, and strength of giant resonances at higher excitation energies. Exploring the excitation energy region above $E_x = 31$ MeV, we have found that locating an $E3$ strength at 75 MeV significantly improves the fit[18] to $A_y(\theta)$ for $\theta > 90°$. This surprising result is highly speculative, and should not be interpreted as the demonstration that a 3^- IGR actually exists in the vicinity of $E_x = 75$ MeV.

Nevertheless, one cannot ignore that a large amount of $E3$ strength is missing above 31 MeV excitation energy. It is unlikely that the suggested 3^- ($E_x \simeq 75$ MeV) state is a simple particle-hole (i.e., RPA) excitation, since it is located at too high an excitation energy.[54,55] On the other hand, it is interesting that this excitation energy is very close to that ($E_x \simeq 80$ MeV) of one of the structures observed in ^{40}Ca + ^{40}Ca collisions at 400 MeV.[56] The origin of these structures is not completely understood,[57] however it is quite possible that they might be interpreted in terms of target multiphonon excitations built on giant resonances.[58] Further experimental explorations of the excitation energy region well above 31 MeV would certainly be very useful in the identification of new collective excitations in ^{40}Ca.

IV. SUMMARY

The new (n,n) and (n,n′) scattering measurements performed at TUNL for $\sigma(\theta)$ and $A_y(\theta)$ between 11 and 17 MeV have been combined with other neutron data available up to 80 MeV to trace the properties of the local OMP for the n + ^{40}Ca system over a broad energy range. From this analysis based on the coupled-channel formalism, we have mapped the interplay between surface and volume absorption.

Additional information on this W_d-W_v interplay is gained from the wealth of (p,p) scattering measurements for $\sigma(\theta)$ and $A_y(\theta)$ available up to 80 MeV. The spin-orbit potential has been determined to be spherical and complex, and its imaginary part is energy-dependent and positive at incident energies below 50 MeV and negative at higher energies. This property cannot be explained by nuclear matter theory. It is also at variance with the Dirac phenomenology. Comparing (n,n′) and (p,p′) scattering, it is found that the collective excitations in ^{40}Ca do not depend upon the isospin structure of the probe.

Coupling to giant resonances has minor effects on the $\sigma(\theta)$ and $A_y(\theta)$ predictions for elastic scattering above 40 MeV. Therefore, it does not seem to be of key importance in solving the long-standing problem (i.e., backward-angle anomaly) observed in elastic scattering from ^{40}Ca in this energy range. On the other hand, this coupling certainly improves the description of the nucleon elastic scattering observables at lower incident energies. In this context, corrections to the real potential induced by dispersion relations have been found to substantially alter and sometimes improve the optical model predictions for elastic scattering. More elaborate conclusions concerning the importance of these corrections to the optical model predictions might be obtained from a reanalysis of the scattering measurements, incorporating precise information on the surface term of the scattering potential as induced by dispersion relations.

ACKNOWLEDGMENTS

We gratefully acknowledge the assistance of H. G. Pfützner and M. L. Roberts during the experiments and in the data analysis. This work was supported by the U.S. Department of Energy, Office of High Energy and Nuclear Physics, under Contract No. DE-AC05-76ER01067.

[1]B. C. Clark, S. Hama, and R. L. Mercer, in *The Interaction Between Medium Energy Nucleons in Nuclei—1982 (Indiana University),* Proceedings of the Interaction Between Medium Energy Nucleons in Nuclei, AIP Conf. Proc. No. 97, edited by H. O. Meyer (AIP, New York, 1982), p. 260.

[2]J. Rapaport, Phys. Lett. **92B**, 233 (1980).

[3]W. Tornow, E. Woye, G. Mack, C. E. Floyd, K. Murphy, P. P. Guss, S. A. Wender, R. C. Byrd, R. L. Walter, T. B. Clegg, and H. Leeb, Nucl. Phys. **A385**, 373 (1982).

[4]C. Mahaux and H. Ngô, Nucl. Phys. **A378**, 205 (1982).

[5]D. E. Bainum, R. W. Finlay, J. Rapaport, J. D. Carlson, and W. G. Love, Phys. Rev. C **16**, 1377 (1977); Nucl. Phys. **A330**, 15 (1979).

[6]J. Raynal, computer code ECIS79 (unpublished); IAEA Report No. IAEA-SMR-8/8, 1972, p. 75.

[7]P. Harihar, K. K. Seth, D. Barlow, S. Iversen, M. Kaletka, H. Nann, A. Saha, C. F. Williamson, J. W. Wong, M. Deady, and W. J. Gerace, Phys. Rev. Lett. **53**, 152 (1984).

[8]T. Tamura, Rev. Mod. Phys. **37**, 679 (1965).

[9]H. Sherif and J. S. Blair, Phys. Lett. **26B**, 489 (1968); see also Refs. 4 and 6.

[10]J. P. Delaroche, S. M. El-Kadi, P. P. Guss, C. E. Floyd, and R. L. Walter, Nucl. Phys. **A390**, 541 (1982).

[11]D. I. Garber and R. R. Kinsey, Brookhaven National Laboratory Report No. BNL-325, 1976, 3rd ed., Vol. 2.

[12]D. C. Larson, D. M. Hetrick, and J. A. Harvey, Bull. Am. Phys. Soc. **25**, 543 (1980).

[13]R. P. DeVito, S. M. Austin, W. Sterrenburg, and U. E. P. Berg, Phys. Rev. Lett. **47**, 628 (1981); and private communication.

[14]F. A. Brieva and J. R. Rook, Nucl. Phys. **A297**, 206 (1978).

[15]C. W. DeJager, H. DeVries, and C. DeVries, At. Data Nucl. Data Tables **14**, 479 (1974).

[16]R. R. Scheerbaum, Nucl. Phys. **A257**, 77 (1976).

[17]J. Dechargé, Commissariat a L'Energie Atomique Report No. CEA-N-2260, 1982, p. 147.

[18]G. M. Honoré, Ph.D. dissertation, Duke University, 1986.

[19]P. Schwandt, H. O. Meyer, W. W. Jacobs, A. D. Bacher, S. E. Vigdor, M. D. Kaithchuck, and T. R. Donoghue, Phys. Rev. C **26**, 55 (1982).

[20]R. L. Walter, W. Tornow, P. P. Guss, and J. P. Delaroche, in *Neutron-Nucleus Collisions—A Probe of Nuclear Structure—1984 (Burr Oak State Park, Ohio),* Proceedings of the Workshop on Neutron-Nucleus Collisions—A Probe of Nuclear Structure, AIP Conf. Proc. No. 124, edited by J. Rapaport, R. W. Finlay, S. M. Grimes, and F. S. Dietrich (AIP, New York, 1985), p. 312.

[21]J. P. Delaroche, P. P. Guss, G. M. Honoré, C. R. Howell, D. C. Larson, D. M. Hetrick, and J. A. Harvey, see Ref. 20, p. 310.

[22]P. M. Endt, At. Data Nucl. Data Tables **23**, 3 (1979).

[23]D. J. Baugh, J. C. Dore, G. W. Greenlees, J. Lowe, and S. Roman, Nucl. Phys. **65**, 33 (1965).

[24]E. T. Boschitz, R. W. Bercaw, and J. S. Vincent, Phys. Lett. **13**, 322 (1964).

[25]K. H. Bray, K. S. Jayaraman, G. A. Moss, W. T. H. van Oers, D. O. Wells, and Y. I. Wu, Nucl. Phys. **A167**, 57 (1971).

[26]C. R. Gruhn, T. Y. T. Kuo, C. J. Maggiore, H. McManus, F. Petrovich, and B. M. Preedom, Phys. Rev. C **6**, 915 (1972).

[27]D. L. Watson, J. Lowe, J. C. Dore, R. M. Craig, and D. J. Baugh, Nucl. Phys. **A92**, 193 (1967).

[28]R. M. Craig, J. C. Dore, G. W. Greenlees, J. S. Lilley, J. Lowe, and P. C. Rowe, Nucl. Phys. **58**, 515 (1964).

[29]B. W. Ridley and J. F. Turner, Nucl. Phys. **58**, 497 (1964).

[30]V. Hnizdo, O. Karban, J. Lowe, G. W. Greenlees, and W. Makofske, Phys. Rev. C **3**, 1560 (1971).

[31]E. E. Gross, R. H. Bassel, L. N. Blumberg, B. J. Morton, A. van der Woude, and A. Zucker, Nucl. Phys. **A102**, 673 (1967).

[32]L. N. Blumberg, E. E. Gross, A. van der Woude, A. Zucker, and R. H. Bassel, Phys. Rev. **147**, 812 (1966).

[33]R. M. Craig, J. C. Dore, J. Lowe, and D. L. Watson, Nucl. Phys. **86**, 113 (1966).

[34]C. B. Fulmer, J. B. Ball, A. Scott, and L. Whiten, Phys. Rev. **181**, 1565 (1969).

[35]H. Sakaguchi, M. Nakamura, K. Hatanaka, A. Goto, T. Noro, F. Ohtani, H. Sakamoto, H. Ogawa, and S. Kobayashi, Phys. Rev. C **26**, 944 (1982).

[36]M. Yosoi, N. Isshiki, H. Sakaguchi, M. Nakamura, H. Ogawa, T. Ichihara, M. Ieiri, Y. Takeuchi, and S. Kobayashi, RCNP Progress Report, Osaka University, 1983 (unpublished), p. 8.

[37]C. Rolland, B. Geoffrion, N. Marty, M. Morlet, B. Tatischeff, and A. Willis, Nucl. Phys. **80**, 625 (1966).

[38]W. T. H. van Oers, Phys. Rev. C **3**, 1550 (1971).

[39]A. Nadasen, P. Schwandt, P. P. Singh, W. W. Jacobs, A. D. Bacher, P. T. Debevec, M. D. Kaitchuck, and J. T. Meek, Phys. Rev. C **23**, 1023 (1981).

[40]N. J. DiGiacomo, R. M. DeVries, and J. C. Peng, Phys. Rev. Lett. **45**, 527 (1980), and references therein.

[41]J. P. Jeukenne, A. Lejeune, and C. Mahaux, Phys. Rev. C **16**, 80 (1977).

[42]E. Fabrici, S. Micheletti, M. Pignanelli, F. G. Resmini, R. De Leo, G. D'Erasmo, and A. Pantaleo, Phys. Rev. C **21**, 844 (1980).

[43]V. A. Madsen and V. R. Brown, see Ref. 20, p. 171.

[44]H. P. Gubler, U. Kiebele, H. O. Meyer, G. R. Plattner, and I.

Sick, Phys. Lett. **74B**, 202 (1978).

[45]F. K. Vosniakos, N. E. Davidson, W. R. Falk, O. Abou-Zeid, and S. P. Kwan, Nucl. Phys. **A332**, 157 (1979); A. M. Kobos and R. S. Mackintosh, J. Phys. G **5**, 97 (1979).

[46]S. Kosugi and Yoshida, Phys. Lett. **106B**, 353 (1981); R. S. Mackintosh, Nucl. Phys. **A230**, 195 (1974); R. S. Mackintosh and A. M. Kobos, Phys. Lett. **62B**, 127 (1977).

[47]R. Alarcon, J. Rapaport, D. Wang, and Y. Wang, Bull. Am. Phys. Soc. **30**, 796 (1985).

[48]M. Pignanelli, H. V. von Geramb, and R. DeLeo, Phys. Rev. C **24**, 369 (1981).

[49]F. E. Bertrand, G. R. Satchler, D. J. Horen, and A. van der Woude, Phys. Lett. **80B**, 198 (1979).

[50]T. A. Carey, W. D. Cornelius, N. J. DiGiacomo, J. M. Moss, G. S. Adams, J. B. McClelland, G. Pauletta, C. Whitten, M. Gazzaly, N. Hintz, and C. Glashausser, Phys. Rev. Lett. **45**, 239 (1980).

[51]J. P. Delaroche, M. S. Islam, and R. W. Finlay, submitted to Phys. Rev. C.

[52]A. B. Smith, P. T. Guenther, and R. D. Lawson, Argonne National Laboratory Report ANL/NDM-91, 1985.

[53]R. W. Finlay, J. R. M. Annand, and J. S. Petler, Phys. Lett. **155B**, 313 (1985).

[54]J. Dechargé and L. Sips, Nucl. Phys. **A407**, 1 (1983); J. Dechargé, private communication.

[55]N. Van Giai, Phys. Lett. **105B**, 11 (1981).

[56]N. Frascaria, P. Colombani, A. Gamp. J. P. Garron, M. Riou, J. C. Roynette, C. Stephan, A. Ameaume, C. Bizard, J. L. Laville, and M. Louvel, Z. Phys. A **294**, 167 (1980).

[57]H. Flocard and M. S. Weiss, Phys. Lett. **105B**, 14 (1981).

[58]Ph. Chomaz, Y. Blumenfeld, N. Frascaria, J. P. Garron, J. C. Jacmart, J. C. Roynette, W. Bohne, A. Gamp, W. Von Oertzen, Nguyen van Giai, and D. Vautherin, Z. Phys. A **319**, 167 (1984).